5.1. INTRODUCTION

Friction and wear are the predominant factors leading to energy depletion and eventual malfunction across almost all mechanical systems, significantly impacting industrial production and various aspects of people's daily lives.[1] Therefore, minimizing friction and wear in mechanical systems in motion is widely acknowledged as a fundamental element in saving energy and protecting the environment.[2] Furthermore, statistical data from Oak Ridge National Laboratory (USA) indicate that approximately 25% of the global energy loss can be attributed to friction or wear.[2]

Managing friction on a nanoscale has become a significant area of research in the present scenario. Nanomaterials exhibiting exceptional mechanical characteristics, thermal stability, and substantial specific surface area have found extensive application as additives for enhanced tribological performance.[3] Owing to their unique physical (great flexibility and mechanical strength) and chemical attributes, two-dimensional (2D) layered materials, including graphene, metal chalcogenides, graphitic carbon nitride, and layered metal hydroxides, displayed remarkable tribological characteristics.[4-11] Their capacity for smooth interlayer sliding, attributed to the weak Van der Waals forces resulting in low shear strengths, makes them extremely attractive as wear and friction-reducing additives to lubricants.[2]

In recent years, oxysalts (including sulfates, chromates, molybdates, tungstates, and vanadates) have garnered growing attention due to their extraordinary lubricating characteristics, attributed to their high ductility and reduced shear strength, particularly at elevated temperatures.[12-14,9,15] Among them, metal vanadates are well known for their remarkable capacity to act as exceptionally effective photocatalysts in water oxidation.[16] They possess encouraging potential in photoelectrochemical processes for water splitting and have also demonstrated prospective applications in tribology.[17,18,15] The potential of silver vanadates (AgV_xO_y) as solid lubricants for high-temperature applications has been explored.[19] The friction coefficient of the NiCr and $AgVO_3$ composite was measured as 0.30 when tested at a temperature of 800 °C.[20] Incorporating Ag_3VO_4 into a NiAl-based composite led to a significantly reduced friction coefficient of 0.06 and a wear rate of 1.08×10^{-5} $mm^3/(Nm)$.[21] $CeVO_4$ nanoparticles were used by Fengzhen et al. as additives for enhancing lubrication in liquid paraffin.[22] Our research group has recently analyzed the tribological characteristics of m-$LaVO_4$ nanoparticles.[23]

Manganese vanadate (MnV_2O_6) has promising applications in various fields like lithium-ion batteries, supercapacitors, photocatalysis, and electrochemical sensors, due to its distinct features, such as a large specific surface area, high chemical and thermal stability, electrical conductivity, narrow bandgap, cost-effectiveness, reversible capacity, and eco-friendliness.[24-28] However, the tribological behavior of MnV_2O_6 has not been explored. The current situation has sparked our interest in studying the lubricant behavior of two-dimensional MnV_2O_6 nanosheets.

According to literature reports, doped nanomaterials introduce defects that create slip systems, resulting in altered electronic structures and reduced shear strength, eventually improving tribological properties.[9,29] Our group has reported notable improvement in the lubricant behavior of paraffin oil using Mg-doped zinc oxide, N-doped zinc oxide, La-doped yttria, La-doped zinc borate, and Ce-doped zirconia as doped nanomaterials.[30,10,6,31,29] Therefore, the present research project aimed to design Cobalt-doped 2D MnV_2O_6 nanosheets for enhanced tribological properties successfully.

The fascinating properties of nanospheres have captured the attention of researchers across diverse fields, including batteries, supercapacitor electrodes, photocatalysis, biosensing, gas-sensing, etc.[32-36] The distinctive spherical structure of nanospheres offers significant benefits, especially in lubrication, due to their ability to act as ideal rolling bearings during lubrication, and keep the tribo-pairs separated, effectively reducing friction and wear.[37] An investigation was carried out by Xue et al. to study the tribological behavior of $MoSe_2$ hollow nanospheres as additives in 100SN base oil.[38] Qian and coworkers assessed the tribological properties of 500SN base oil incorporating nitrogen-phosphorus co-doped carbon nanospheres as additives.[1] Porous carbon nanospheres (PCNs), core-shell Ag@C nanospheres, cerium borate nanospheres, Fe_3O_4 nanospheres, and MoS_2 nanospheres have been extensively employed for friction reduction.[39-42,2] Recently, nickel oxide (NiO) has gained special recognition for its remarkable lubrication properties.[43-46] Based on the above finding, it was speculated that the NiO nanospheres could potentially enhance the tribological performance of the base oil.

Due to the well-established nano effect, which involves high surface energy and van der Waals interactions, nano additives readily aggregate in most base oils.[39] Fabricating a nanomaterial composite could be a viable approach to resolving the agglomeration issue.[3] Spherical and lamellar nanomaterials are frequently employed in composite fabrication to improve the tribological properties; for instance, graphene/h-BN nanosheet/nanosphere composites, graphene oxide (GO)-wrapped SiO_2 nanosphere modified with a 1-methylimidazolium bis(salicylato)borate (MEIMBScB) ionic liquid, etc.[47,3]

The captivating literature reports mentioned above inspired us to improve the tribological properties of Co-MnV_2O_6 nanosheets(C-MVO) by creating a composite material with a metal-organic framework (MOF)-derived NiO nanospheres called NiO/C-MVO. Consequently, the synthesis of MnV_2O_6 (MVO) nanosheets, Co-MnV_2O_6 (C-MVO) nanosheets, NiO nanospheres, and the NiO/Co-MnV_2O_6 (NiO/C-MVO) composite was carried out. Their tribological performance was evaluated in paraffin oil (PO) using a four-ball tester machine following the ASTM D4172 and ASTM D5183 testing conditions.

5.2. EXPERIMENTAL SECTION

5.2.1. Materials

During the ongoing investigation, chemicals of the Analytical Reagent grade that were utilized were acquired from Merck India.

5.2.2. Syntheses of nano additives

5.2.2.1. Synthesis of pure manganese vanadate (MnV_2O_6) and Co-doped MnV_2O_6 nanosheets

A hydrothermal method was employed to synthesize both pure MnV_2O_6 (MVO) and Co-doped MnV_2O_6 (C-MVO) nanosheets.[48] At 70 °C, a yellow solution A was formed by dissolving 4.8 mmol NH_4VO_3 in 37.0 mL of deionized water with continuous stirring. Subsequently, a clear solution was achieved by continuously stirring 0.5 g of polyvinyl pyrrolidone (PVP) in deionized water (10.0 mL) at room temperature. To this solution, a mixture of $MnCl_2·4H_2O$ and $CoCl_2·6H_2O$ with a molar ratio of 9:1 (2.4 mmol) was added, resulting in solution B. Afterward, solution B was carefully added drop by drop to solution A to ensure a homogeneous solution and then transferred into a PTFE-lined autoclave (50 mL) and subjected to an 18 h heat treatment at 200 °C in an oven. The product (C-MVO) was obtained after centrifugation, followed by multiple washings and drying at 65 °C for a 10 h duration. In the preparation of pure MnV_2O_6, a similar procedure was followed, excluding the inclusion of $CoCl_2·6H_2O$ (0.24 mmol) in the reaction mixture.

5.2.2.2. Synthesis of MOF-derived NiO nanospheres

In the synthesis process, a mixture containing $Ni(NO_3)_2·6H_2O$ (0.02 M, 20 ml) in N, N-dimethylformamide (DMF) solution, 1,4-benzenedicarboxylic acid (BDC) (25 mg) and ethylene glycol (6 ml) was vigorously stirred at room temperature for a duration of 30 min. Subsequently, the resulting solution was moved into a Teflon-lined autoclave with a capacity of 50 ml and held at 120 °C for a duration of 6 hours. Upon gradual cooling to room temperature, centrifugation was performed to obtain the light green precipitate which was collected after undergoing multiple washes with DMF and anhydrous ethanol before being dried at 60 °C for a period of 12 h. Afterward, the aforementioned greenish precipitate was subjected to calcination at 400 °C for 1 hour in the presence of air, using a ramp rate of 1 °C min^{-1}. As a result, the color of the product transformed from greenish to black.[49]

5.2.2.3. Preparation of binary nanocomposite, NiO/C-MVO

Separate dispersions of C-MVO nanosheets (300 mg) and NiO nanospheres (200 mg) were prepared in 50 mL of ethanol each through ultrasonication for 30 min at approximately 50 °C. After preparing the individual dispersions, they were combined and subjected to reflux at 80 °C with continuous stirring for 24 h. Once the reaction mixture reached room temperature, it underwent filtration and was subsequently dried at 60 °C. Ultimately, a nanohybrid NiO/C-MVO was obtained, exhibiting a grayish-brown appearance.

Scheme 5.1 depicts the schematic illustration of the comprehensive synthesis process for the nanohybrid NiO/C-MVO.

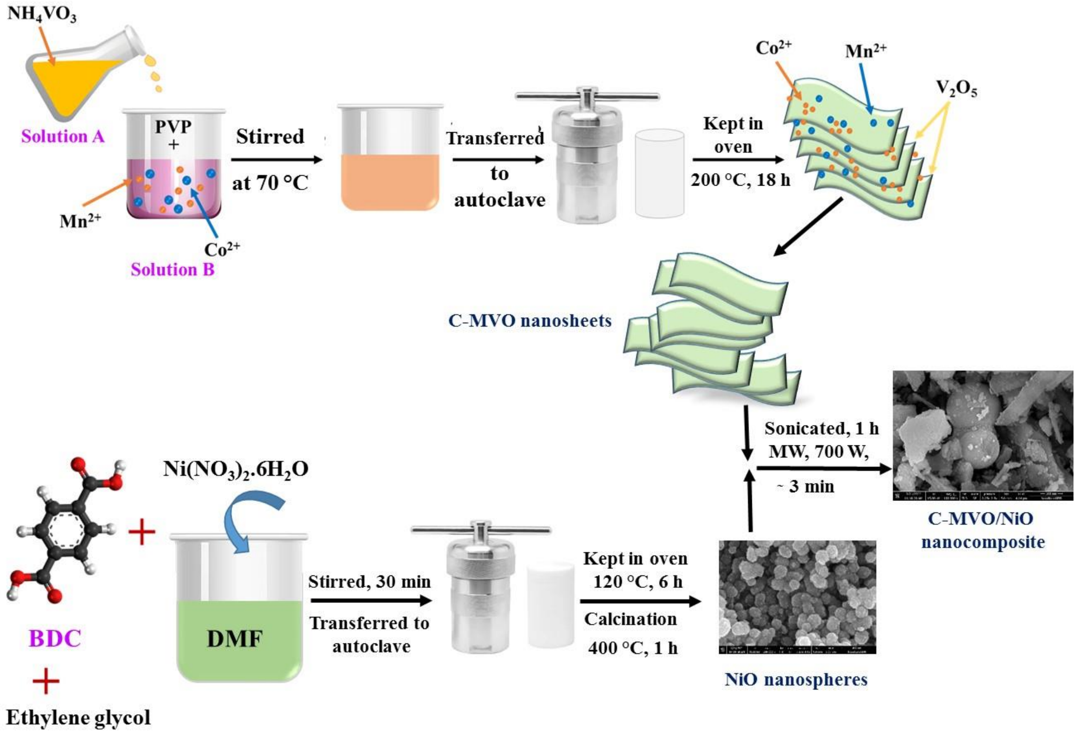

Scheme 5.1. Schematic representation illustrating the procedure for NiO/C-MVO fabrication

5.2.2.4. Sample preparation

Test samples of the as-prepared additives were made in PO with varying concentrations;

0.000, 0.025, 0.050, 0.075, and 0.100% w/v by sonicating at room temperature for 1h. The antiwear and load ramp tests for all these mixtures were executed on a Ducom four-ball tester, following the ASTM D4172 and ASTM D5183 regulations, correspondingly.

5.3. RESULTS AND DISCUSSION

5.3.1. Techniques adopted to characterize the nano additives *MVO, C-MVO, NiO, and the hybrid NiO/C-MVO*

The as-prepared additives were examined by utilizing XRD, FT-IR, SEM/HR-SEM, TEM/HR-TEM, XPS, and UV/visible. The XRD patterns of MVO, C-MVO, NiO, and NiO/C-MVO are shown in Figure 5.1a. The obvious diffraction peaks at 27.02°, 27.80°, 28.96°, 32.37°, 38.31°, 51.42°, 59.49° and 60.75° corresponding to the planes (110), (-202), (201), (111), (-311), (020), (-222), and (402) of MVO (JCPDS 72-1837) respectively could be indexed for the brannerite structure.[48] The brannerite crystallites extend in C-MVO but the relative positions of XRD peaks shift toward a higher value compared with the pure MVO, evidencing the effective Cobalt doping in MVO.[48] The XRD pattern of NiO (face-centered cubic phase) exhibiting peaks corresponding to the planes (111), (200), (220), (311), and (222) followed the JCPDS card No. 47-1049.[49,50] The heterostructure NiO/C-MVO exhibited all the characteristic diffraction peaks of C-MVO and NiO, suggesting the successful formation of hybrid.

The additives were put through FT-IR analysis, as shown in Figure 5.1b, to further corroborate the successful synthesis of lubricant additives. The FT-IR spectrum of NiO divulged stretching vibration band at 455 cm^{-1} is ascribed to the Ni-O bond.[51] In the spectrum of MVO, the characteristic peaks are visible in the range of 500-900 cm^{-1} which commensurate to the symmetric and asymmetric stretching vibrations of V-O-V bonds.[52] The absorption peak at 568 cm^{-1} is assignable to the stretching mode of the Mn-O bond.[52] Analogous peaks were evident in the IR spectrum of C-MVO.[52] In the FTIR spectrum of the hybrid NiO/C-MVO, the prominent C-MVO peaks were maintained and also features the main distinctive peaks of NiO, demonstrating the substantial interaction of C-MVO and NiO in the composite.

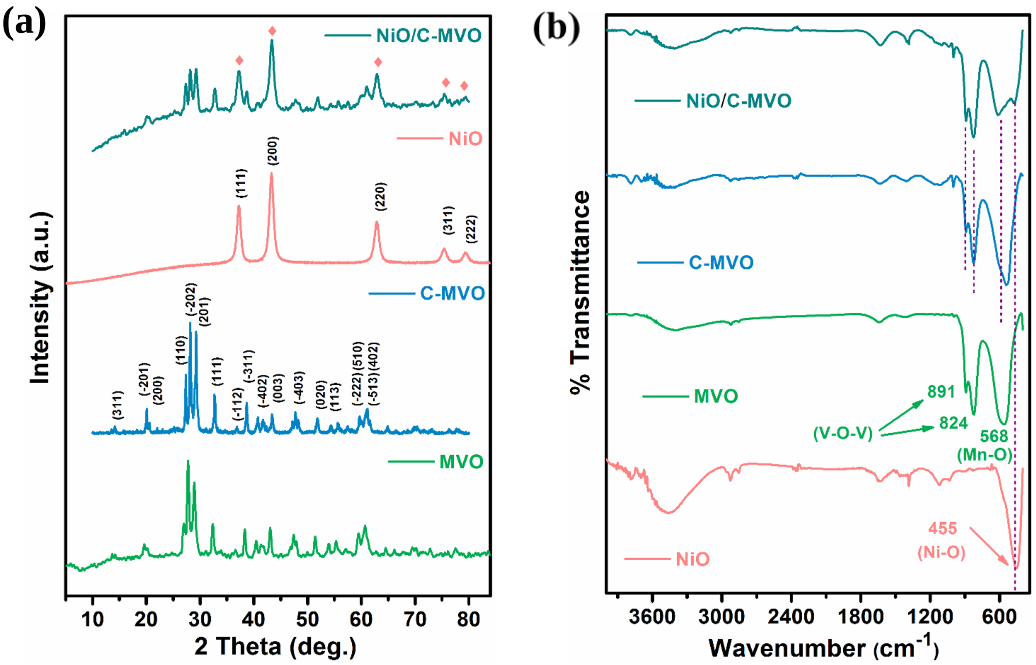

Figure 5.1. (a) XRD patterns and (b) IR spectra of MVO, C-MVO, NiO, and NiO/C-MVO

For analyzing the morphology and microstructure of MVO, C-MVO, NiO, and NiO/C-MVO, HR-SEM images were captured and depicted in Figure 5.2a-d respectively. In Figure 5.2a and b, the nanosheets of MVO and C-MVO are observable showing the resemblance with accordion morphology. Nanosheets of MVO and C-MVO, exhibiting lateral dimensions in the range 400 nm-3μm and 300 nm-1000 nm, respectively. The thickness was measured as 30 nm-70 nm and 30 nm-50 nm for MVO and C-MVO nanosheets respectively, using Image J software. It is noticeable in Figure 5.2c, that NiO exhibits a consistent 3D nanosphere morphology which has been constructed from closely packed nanoparticles, having 150-250 nm diameter on average. The NiO nanosphere embellished C-MVO nanosheets were featured in Figure 5.2d.

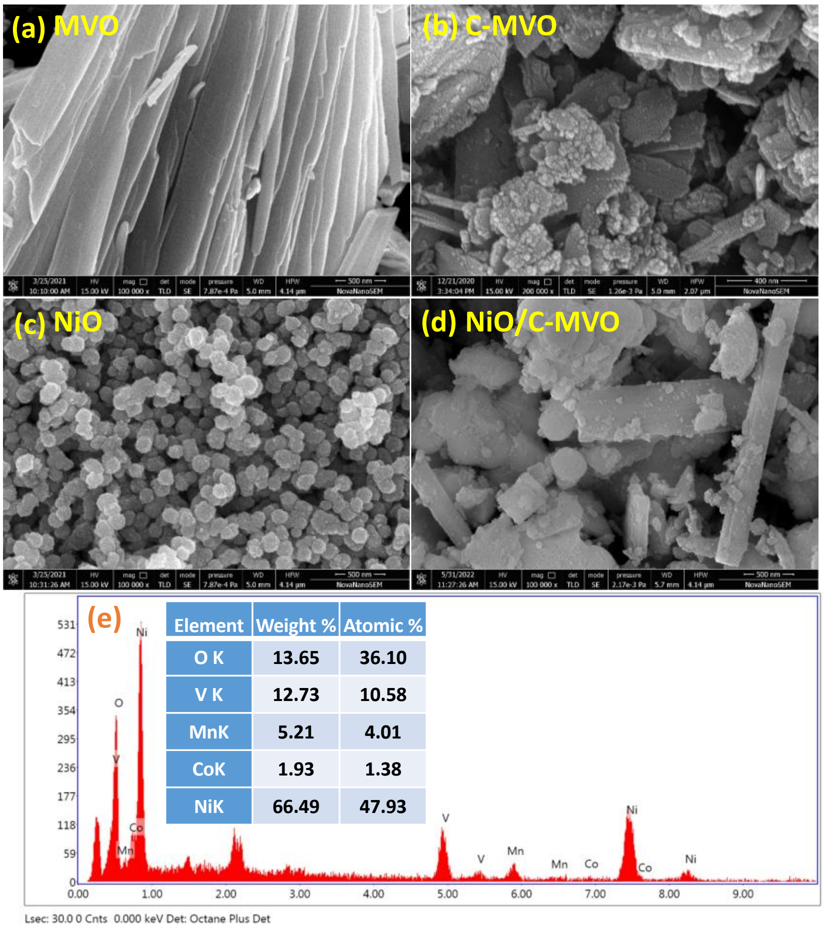

Element	Weight %	Atomic %
O K	13.65	36.10
V K	12.73	10.58
MnK	5.21	4.01
CoK	1.93	1.38
NiK	66.49	47.93

Figure 5.2. HR-SEM photographs of (a) MVO, (b) C-MVO, (c) NiO, (d) NiO/C-MVO, and (e) EDX spectrum of NiO/C-MVO

The EDX spectrum of hybrid NiO/C-MVO, corroborated in Figure 5.2e validates the elemental components nickel, cobalt, manganese, vanadium, and oxygen. The existence of these elements provides proof for the formation of nanocomposite. EDX spectra of MVO, C-MVO, and NiO are furnished in Figure 5.3.

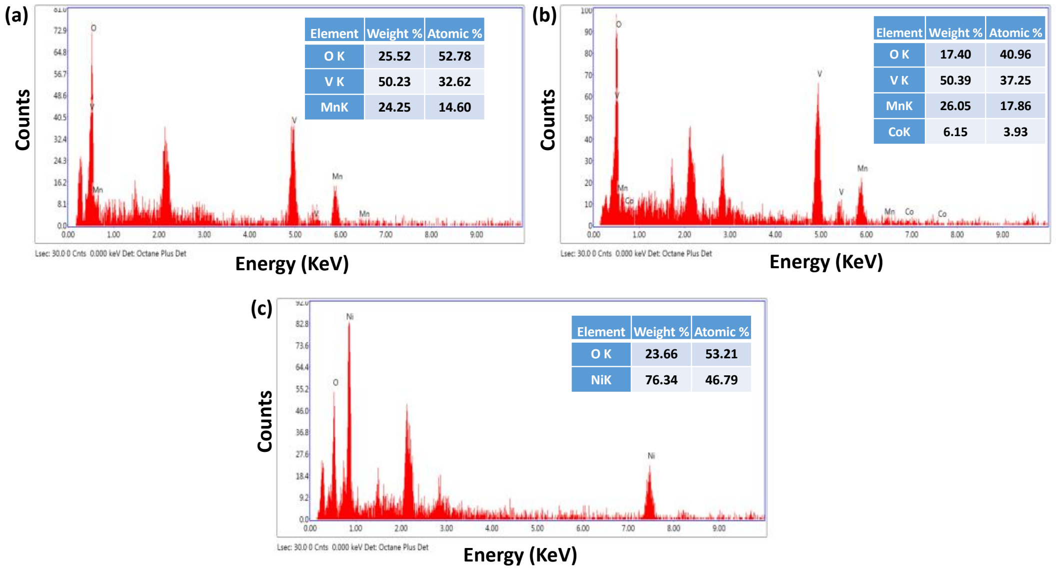

(a)

Element	Weight %	Atomic %
O K	25.52	52.78
V K	50.23	32.62
MnK	24.25	14.60

(b)

Element	Weight %	Atomic %
O K	17.40	40.96
V K	50.39	37.25
MnK	26.05	17.86
CoK	6.15	3.93

(c)

Element	Weight %	Atomic %
O K	23.66	53.21
NiK	76.34	46.79

Figure 5.3. EDX spectrum of, (a) MVO, (b) C-MVO, and (c) NiO

For a more apparent perception of morphological traits, TEM images of nanomaterials MVO, C-MVO, NiO, and NiO/C-MVO were also manifested and visualized in Figure 5.4a-d, respectively. Figures 5.4a and b shows the TEM images of MVO and C-MVO which are made up of 2D nanosheet units. The HR-TEM picture of MVO and C-MVO (Figures 5.4a$_1$ and 5.4b$_1$) illustrates lattice fringes as 0.32 nm and 0.31 nm, respectively corresponding to the plane (110).[48] Significant crystallinity can be seen in the selected area diffraction (SAED) patterns of MVO and C-MVO, which is illustrated in the inset of the respective Figures (5.4a$_1$ and 5.4b$_1$). The nanosphere structure of NiO is clearly visible in Figure 5.4c, with an interplanar spacing of 0.21 nm allied with the (200) crystal plane as depicted in Figure 5.4c$_1$.[53] The SAED pattern of NiO nanosphere is illustrated in the inset of corresponding Figure, confirm the polycrystalline character of the material.

In Figure 5.4d, NiO nanospheres are uniformly embedded amidst the layered C-MVO nanosheets. In the HR-TEM image of the composite, the lattice fringe spacing of C-MVO nanosheets accordant with the (110) plane has been observed an increment from 0.31 nm to 0.33 nm (Figure 5.4d_1). The fact that the NiO nanosphere interacts favorably with the nanosheets of C-MVO is highlighted by the rise in the interplanar distance of C-MVO nanosheets.[6] The hybrid exhibits significant crystallinity as seen by its SAED pattern shown in the inset of Figure 5.4d_1.

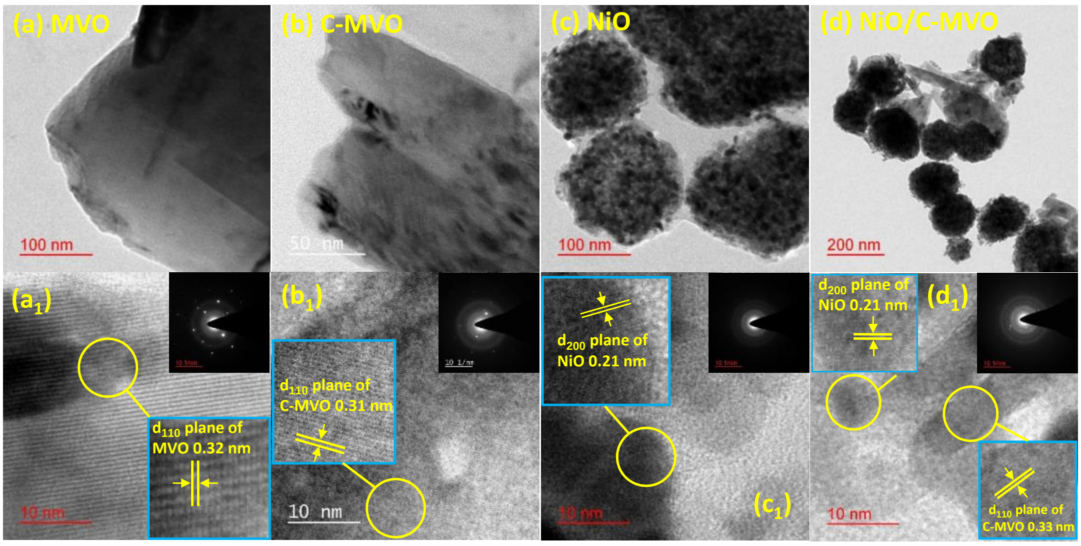

Figure 5.4. TEM photographs of (a) MVO, (b) C-MVO, (c) NiO, (d) NiO/C-MVO, and HR-TEM photographs of MVO (a_1), C-MVO (b_1), NiO (c_1), and NiO/C-MVO (d_1) with SAED patterns in the insets (a_1, b_1, c_1, and d_1)

Utilizing XPS analysis, a thorough examination was carried out to explore the comprehensive elemental characteristics and ascertain the oxidation state of the NiO/C-MVO composite. The deconvoluted core level spectra of Co 1s, Mn 2p, V 2p, Ni 2p, and O 1s, obtained through peak fitting software, are presented in Figure 5.5.

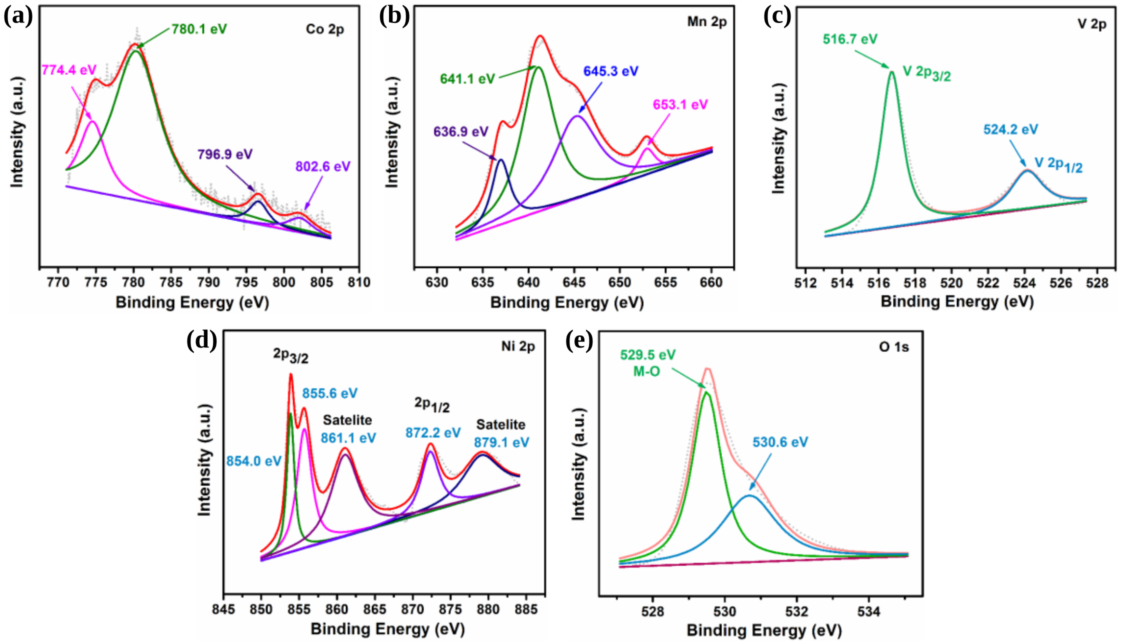

Figure 5.5. Deconvoluted XP spectra of NiO/C-MVO (a) Co 2p, (b) Mn 2p, (c) V 2p, (d) Ni 2p, and (e) O 1s

The Co 2p XP spectrum (Figure 5.5a) exhibits four distinct peaks. Specifically, the presence of Co^{2+} is denoted by the peaks at 786.2 eV and 802.6 eV, whereas the occurrence of Co^{3+} is evidenced by the peaks located at 780.1 eV and 796.9 eV.[48] In Fig. 5.5b, the high-resolution Mn 2p XP spectrum is characterized by the presence of two prominent peaks at 641.1 eV (Mn $2p_{3/2}$) and 653.1 eV (Mn $2p_{1/2}$), along with an additional set of satellite peaks at 645.3 and 657.3 eV. These features are recognized as indicative of Mn^{2+}.[48] The appearance of peaks at 516.7 and 524.2 eV in the V 2p XP spectrum (Figure 5.5c), verified the existence of V^{5+}.[48] As depicted in Figure 5.5d, the deconvolution of Ni 2p XP spectrum reveals four distinct peaks positioned at 854.0, 861.1, 872.2, and 879.1 eV, affirming the presence of NiO.[54] The Ni $2p_{3/2}$ and Ni $2p_{1/2}$ spin–orbit levels are denoted by the prominent peaks observed at 854.0 and 872.2 eV, respectively. In addition, satellite peaks corresponding to Ni $2p_{3/2}$ and Ni $2p_{1/2}$ are evident at energy levels of 861.1 and 879.1 eV.[54] Within the XPS spectrum of O 1s, the fitting curve was differentiated into two separate peaks situated at 529.5 eV and 530.6 eV, associated with lattice oxygen and adsorbed water respectively (Figure 5.5e).[48,6] Consequently, the XPS outcomes validate the formation of hybrid NiO/C-MVO successfully.

5.3.2. Assessment of tribological behavior of nano additives in paraffin oil

5.3.2.1. Dispersion stability

The stability of nano-fluid dispersions is a major consideration for their effective use in tribological applications. The utilization of electronic spectroscopy (UV/visible) has proven beneficial in achieving the stated objective. The base lube was subjected to ultrasonication with the optimized concentration of additives and subsequently diluted by a factor of 10. The measurements of absorbance were recorded for diluted dispersions, over a time span of 0 to 72 h. The relative absorbance of the dispersions is depicted in Figure 5.6a as a function of settling time. The stability of the dispersion can be inferred from the extent of the decrease in relative absorbance over time. The order of dispersion stability, from highest to lowest, is observed in the nanocomposite structure, followed by C-MVO, NiO, and finally MVO.

The inset of Figure 5.6a illustrates the absorbance values of NiO/C-MVO at around 442 nm, for the initial stage as well as after 12, 24, 48, and 72 h. Fig. 5.6b displays sequential snapshots of both the base lubricant and the dispersions on the day 1, 2, and 3.

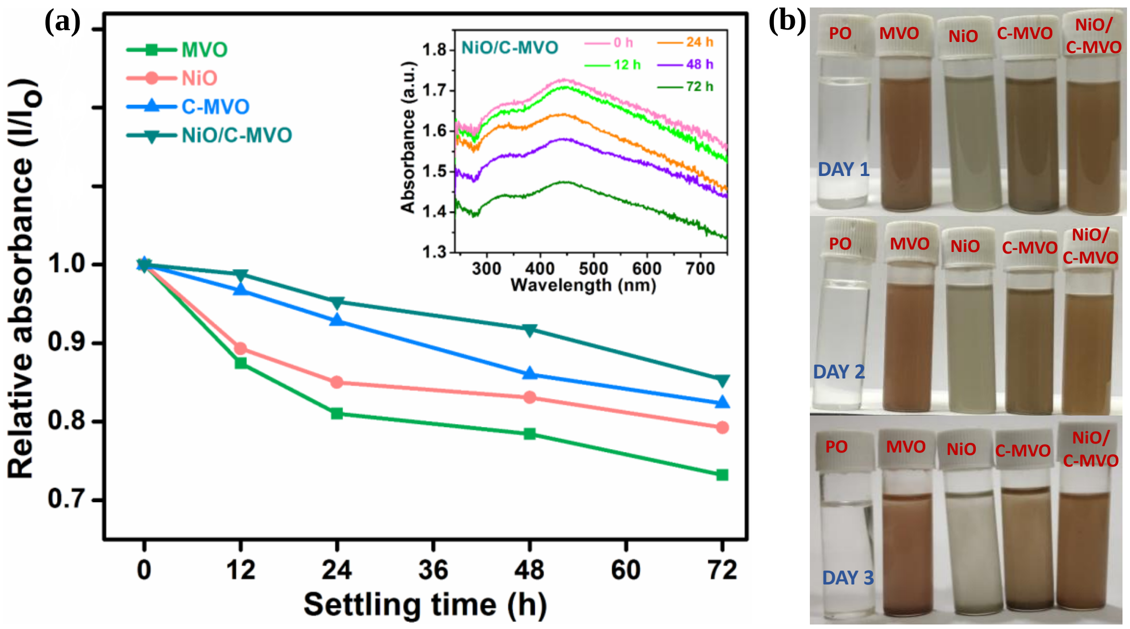

Figure 5.6. (a) Dispersion stabilities of base lube containing MVO, C-MVO, NiO, and NiO/C-MVO using UV-vis spectrophotometry, (b) Photographs of the admixtures from the day 1-3

5.3.2.2. Evaluation of Optimized concentration of the additives

The efficacy of the additives relies significantly on the concentration, making it a crucial variable that needs to be optimized first. The ASTM D4172 standard test was conducted in PO with varying concentrations (0.000%, 0.025%, 0.050%, 0.075%, and 0.100% w/v) of admixtures under a load of 392 N for 60 min at 1200 rpm and the resulting mean wear scar diameters (MWD) were recorded. Figure 5.7a illustrates a plot depicting the relationship between the concentration of the additives and MWD. For all the examined concentrations of the additives, there is a significant decrease in values when compared to the base lube. As a result, it is evident that wear reduction occurs at the tested concentrations for all the additives, although the extent of their antiwear efficacy varies significantly. The MWD value of plain PO was measured as 0.735 mm. All additives exhibited superior performance compared to the base lube. Typically, the MWD shows a reduction up to 0.050% w/v, however, beyond this concentration, the MWD starts to increase, except in the case of MVO and NiO, which exhibited an increase in MWD after reaching 0.025% w/v and 0.075% w/v, respectively. Therefore, the optimized concentration for conducting the tests has been established as 0.050% w/v. Among the various nanoadditives tested, the nanohybrid exhibits the highest level of antiwear performance, as evidenced by the descending order of the variation in MWD for MVO (0.570 mm), NiO (0.533 mm), C-MVO (0.510 mm), and NiO/C-MVO (0.438 mm).

In Figure 5.8, the optimization of COF as a function of additive concentration is presented for all the additives, revealing that the lowest antifriction performance is achieved for NiO/C-MVO at a concentration of 0.050% w/v, C-MVO (0.050% w/v), NiO (0.075% w/v), and MVO (0.025% w/v). At an optimized concentration (0.050% w/v), Fig. 5.7b portrays the changes in the COF over time for the pure PO and its combinations with additives. During the initial stages, the absence of a protective tribofilm results in comparatively higher COF values across all cases. As the in situ tribofilm formation commences, the coefficient of friction (COF) decreases, eventually reaching a stable state upon the completion of the tribofilm formation. The Figure illustrates the presence of irregular COF patterns when additives are absent, while the utilization of additives results in a more consistent and uniform COF. The smoothness of the plot is directly correlated with the characteristics of the tribofilm. In the nanohybrid NiO/C-MVO, nanosheets, and nanospheres have undergone substantial interaction, resulting in the formation of a cohesive, uniform, and stable tribofilm that effectively separates the mating surfaces, leading to noteworthy values for MWD and COF.

5.3.2.3. Friction and wear modifying the behavior of the additives

Antiwear properties of plain PO and its mixtures with various additives were evaluated through the ASTM D4172 test. In Figure 5.7c, the recorded crucially significant parameters, MWD and COF, are concurrently depicted using a bar diagram. The graph clearly indicates a noticeable reduction in the MWD value, starting from plain PO (0.735 mm) and extending to all admixtures, with % reductions in the following order: MVO (22.44%), NiO (27.48%), C-MVO (30.61%), and NiO/C-MVO (40.40%). The decrease in MWD provides a suggestive indication for the effectiveness of the antiwear efficiency. Co-doping in MVO has led to an 8.17% decrease in MWD, indicating an enhancement in its activity compared to MVO.

When assessing the average COF for the various admixtures, a similar trend of % reduction is observed, consistent with the MWD results. Consequently, the presence of additives, MVO (24.09%), NiO (28.90%), C-MVO (41.76%), and NiO/C-MVO (60.31%), results in a significant decrease in the COF of PO (0.0756).

5.3.2.4. Load bearing capacity

To assess the load carrying efficiency, the load ramp test, following ASTM D5183 specifications, was carried out under specified conditions: a load of 392 N, temperature of 75 °C, 600 rpm, and lasting for 1 hour to finish the running-in period at the optimized additive concentration. Subsequently, the steady-state test was performed by progressively increasing the load by 98 N in each 10-minute cycle until reaching the seizure load as a result of an abrupt increase in frictional torque, as depicted in Figure 5.7d. A seizure is observed at the load of 1078 N for the base lube. Afterward, the nearby surfaces become seized, and the resulting load is identified as the seizure load, indicating the additive's ability to bear the load. At the seizure load, the tribofilm experiences significant damage, leading to the failure of the lubricant to withstand the applied load. The findings evidently demonstrate that the rise in seizure load corresponds to the antifriction/antiwear effectiveness of the additives: as observed in MVO (1356 N), NiO (1636 N), C-MVO (2156 N), and NiO/C-MVO (2646 N). Therefore, it is evident that the composite NiO/C-MVO exhibits remarkable load-bearing capability.

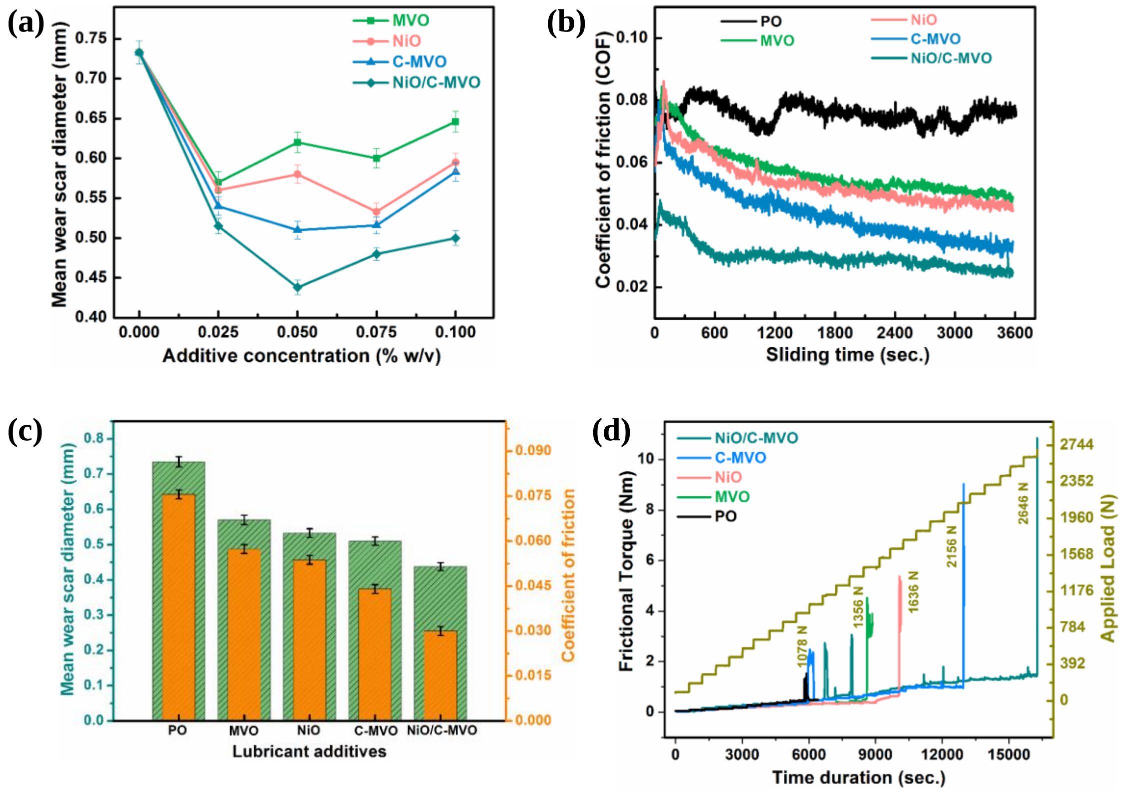

Figure 5.7. (a) MWD vs additive concentration, (b) COF vs sliding time, (c) MWD and COF in the pattern of bar diagram, and (d) Frictional torque against time and load

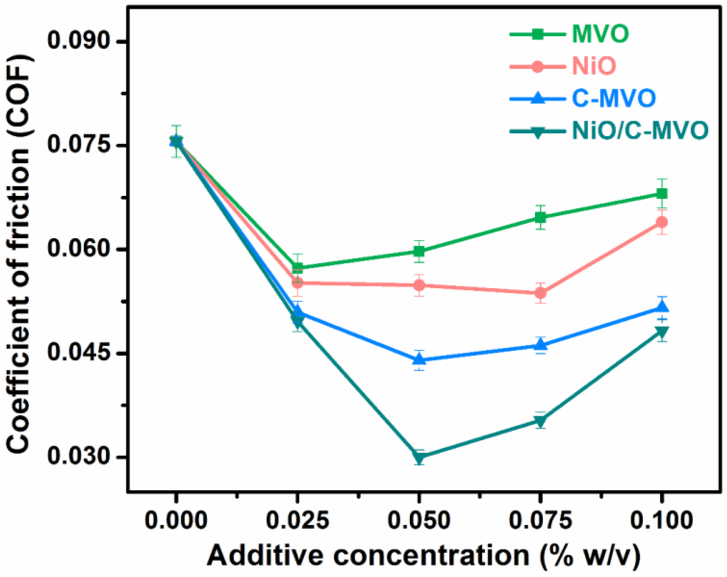

Figure 5.8. Variation of coefficient of friction (COF) vs. additive concentration

5.3.2.5. Frictional Power Loss

Equation (5.1) was employed to assess the power loss (P) resulting from frictional force for the base lubricant with and without the presence of additives.

$$P = 0.221 \times 3.6 \times \mu\, MJ \qquad (5.1)$$

Where μ = coefficient of friction.

The data presented in Table 5.1 reveals that when considering PO alone, a remarkably high value of power consumption (0.0601 MJ) was perceived. However, when blended with different additives, there was a substantial decrease in power consumption in the order: MVO (0.0456 MJ), NiO (0.0427 MJ), C-MVO (0.0350 MJ), and NiO/C-MVO (0.0238 MJ). Consequently, the hybrid (NiO/C-MVO) exhibits the least power consumption, leading to the highest energy preservation.

Table 5.1. Cutbacks in frictional power for individual additives in paraffin oil at the optimized concentration, 0.050 % (w/v).

S. No.	**Additives**	**Power consumption (MJ)**	**Reduction in Power consumption**	**% Reduction in Power consumption**
1.	PO	0.0601	____	____
2.	MVO	0.0456	0.0145	24.12
3.	NiO	0.0427	0.0174	28.95
4.	C-MVO	0.0350	0.0251	41.76
5.	NiO/C-MVO	0.0238	0.0363	60.39

5.3.3. Worn surface Morphological studies

Utilizing surface examination techniques like SEM and AFM, the morphology of the worn track on the steel ball, which had undergone testing with additive blends in accordance with ASTM D4172 standards, was investigated. Figure 5.9 presents the SEM images illustrating the wear scar pathway under lubrication conditions of pure PO as well as its blends with various additives (0.050% w/v).

The SEM micrograph reveals a rugged surface with deep scratches in the case of plain PO, while a noticeably improved surface is evident in the presence of admixtures. The degree of surface enhancement substantiates the sequence of analyzed tribological attributes exhibited by the admixtures. The MWD data supplied in the inset of the pictures exhibit a fairly good agreement with the surface's uniformity. Hence, employing base lube containing hybrid (NiO/C-MVO) for lubrication leads to the attainment of an extraordinarily smooth surface. In Fig. 5.9f, the EDX analysis of the wear track illustrates the presence of all constituent elements of the hybrid, providing confirmation of their active adsorption on the wear track. Figure 5.10 contains the EDX spectrum of wear track lubricated with MVO, C-MVO and NiO.

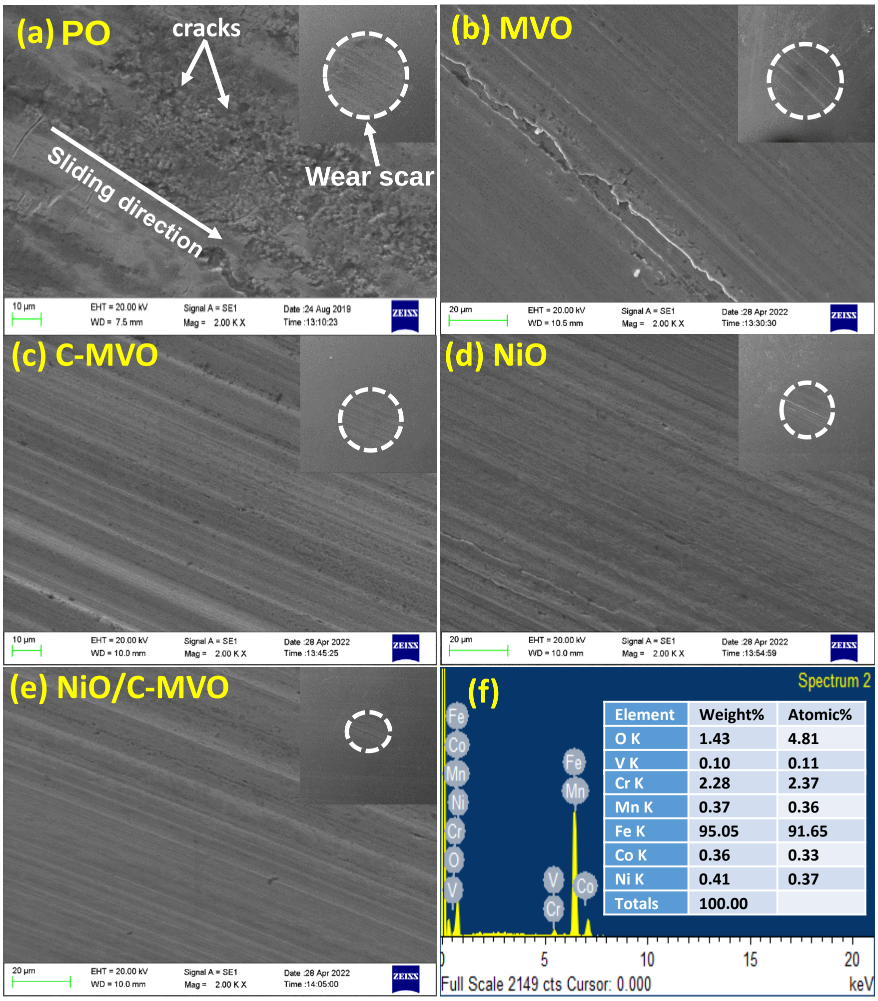

Element	Weight%	Atomic%
O K	1.43	4.81
V K	0.10	0.11
Cr K	2.28	2.37
Mn K	0.37	0.36
Fe K	95.05	91.65
Co K	0.36	0.33
Ni K	0.41	0.37
Totals	100.00	

Figure 5.9. (a)-(e) SEM optical photographs of the wear track surfaces of different admixtures at 2.0 K X amplification, wear scar surfaces in the inset at 100 K X (f) EDX spectrum of wear track surfaces lubricated with NiO/C-MVO

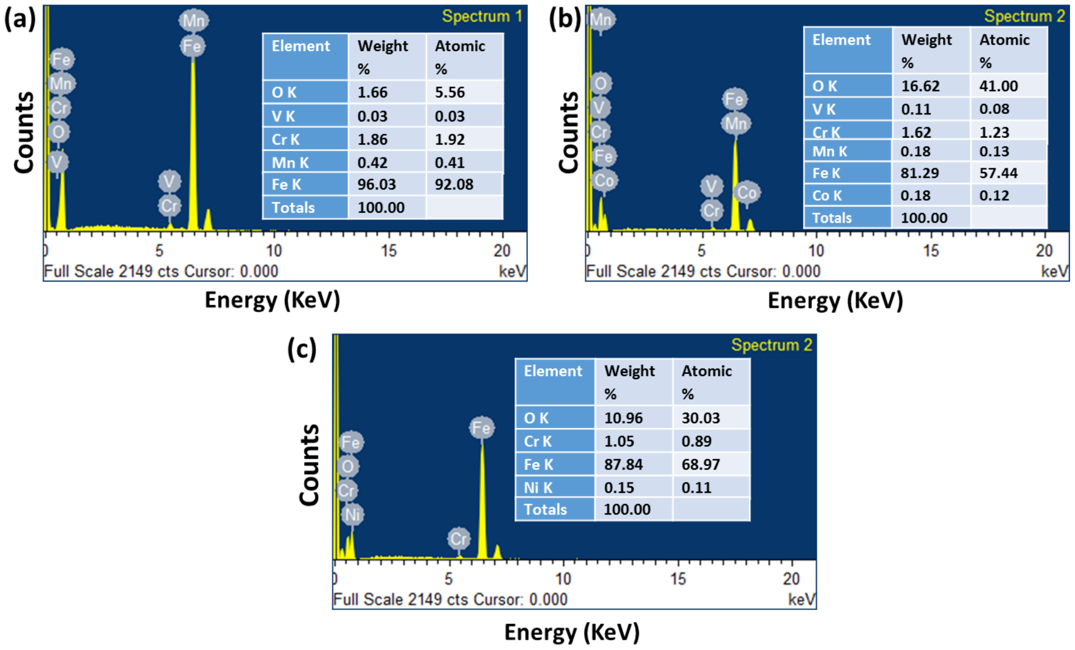

(a)

Element	Weight %	Atomic %
O K	1.66	5.56
V K	0.03	0.03
Cr K	1.86	1.92
Mn K	0.42	0.41
Fe K	96.03	92.08
Totals	100.00	

(b)

Element	Weight %	Atomic %
O K	16.62	41.00
V K	0.11	0.08
Cr K	1.62	1.23
Mn K	0.18	0.13
Fe K	81.29	57.44
Co K	0.18	0.12
Totals	100.00	

(c)

Element	Weight %	Atomic %
O K	10.96	30.03
Cr K	1.05	0.89
Fe K	87.84	68.97
Ni K	0.15	0.11
Totals	100.00	

Figure 5.10. EDX spectrum of wear track of steel surface lubricated with (a) MVO, (b) C-MVO, and (d) NiO

Moreover, the surface roughness of the steel ball, lubricated with plain PO and blends of additives under the ASTM D4172 test, was assessed using contact mode AFM. In Figure 5.11, there are depictions of the worn surfaces through 3D and 2D AFM micrographs. The information regarding surface roughness values corresponding to PO and various admixtures, are demonstrated as area roughness (Sq) and line roughness (Rq) in Figure 5.11. The inclusion of additives MVO, C-MVO, NiO, and NiO/C-MVO in the base oil results in a noteworthy reduction in both Sq and Rq values. The AFM results provided confirmation for the assessments made through SEM analyses and emphasized a distinctly smooth surface with minimal roughness for hybrid NiO/C-MVO. Moreover, supplementary roughness measures including Ra, Rm, Rp, Ry, Rv, Sa, Sm, Sp, Sy, and

Sv have provided additional support to the tribological findings, and these are detailed in Table 5.2.

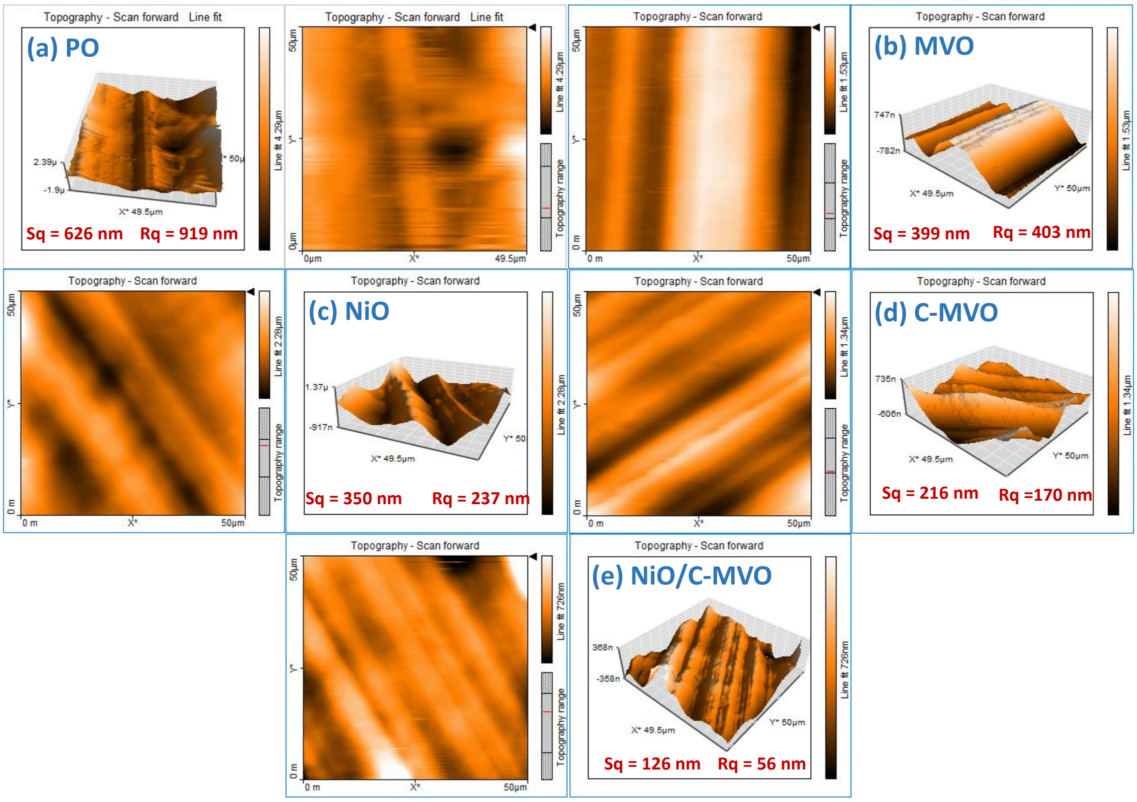

Figure 5.11. 2D and 3D AFM snapshots of the wear track in the presence of PO and its blends at the optimal concentration (0.05% w/v) (a) PO, (b) MVO, (c) NiO (d) C-MVO, and (e) NiO/C-MVO

Table 5.2. Surface roughness parameters obtained from the digital processing software of AFM (Nanosurf-basic Scan-2) for different additives after the antiwear test

Surface roughness parameter	Sq (nm)	Rq (nm)	Sa (nm)	Ra (nm)	Sy (nm)	Ry (nm)	Sp (nm)	Rp (nm)	Sv (nm)	Rv (nm)	Sm (pm)	Rm (pm)
PO	626	919	488	771	4363	3255	2611	2060	-1752	-1195	129	-129
MVO	350	237	282	189	2293	975	1474	526	-819	-448	174	203
NiO	399	403	345	347	1469	1311	726	648	-742	-662	93	58
C-MVO	216	403	171	142	1274	616	730	268	-544	-348	147	218
NiO/C-MVO	126	56	85	47	1630	242	1212	79	-418	-162	130	125

Where, S = Areal roughness, and R = Linear roughness parameters.

Sq = root mean square height, Rq = root mean square line

Sa = Arithmetical mean height, Ra = Arithmetic mean line

Sy = Maximum height of the surface, Ry **=** Maximum height of the profile

Sp **=** Maximum peak height**,** Rp **=** Maximum profile peak height

Sv = Maximum valley depth, Rv = Maximum profile valley depth

Sm = Mean width area, Rm **=** Mean width line

5.3.4. XPS Analysis of Tribofilm

XPS has been employed to analyze the chemical states of the individual components within the tribofilm formed in situ on the worn steel surface, which was lubricated with a composite (NiO/C-MVO), subsequent to undergoing the ASTM D4172 test. Figure 5.12 (a-f) displays the core-level spectra of Co 2p, Mn 2p, V 2p, O 1s, Ni 2p, and Fe 2p, which have been analyzed using peak fit software. The observed peak positions within the XP spectra of Co 2p, Mn 2p, V 2p, O 1s, and Ni 2p indicate the occurrence of tribochemical oxidation, leading to the creation of cobalt oxides (Co_2O_3, Co_3O_4),[55] various manganese oxides (MnO_2, Mn_2O_3),[56] vanadium oxide (VO_2, V_2O_5),[57] and nickel oxides (NiO, Ni_2O_3)[58-60]. Furthermore, within the Fe 2p spectrum, the presence of peaks at 724.7 eV (Fe $2p_{1/2}$) and 711.1 eV (Fe $2p_{3/2}$) indicates the generation of Fe_2O_3 due to the oxidation of the steel ball being tested.[7,10,23] In addition, the peak positioned at approximately 852.8 eV in the Ni 2p spectrum corresponds to metallic nickel, which can be ascribed to the presence of a Ni-Fe/Cr metallic alloy.[61] As a result, the combination of the metallic alloy and various self-lubricating oxides contributes to lubrication, thereby enhancing the tribological performance of NiO/C-MVO.

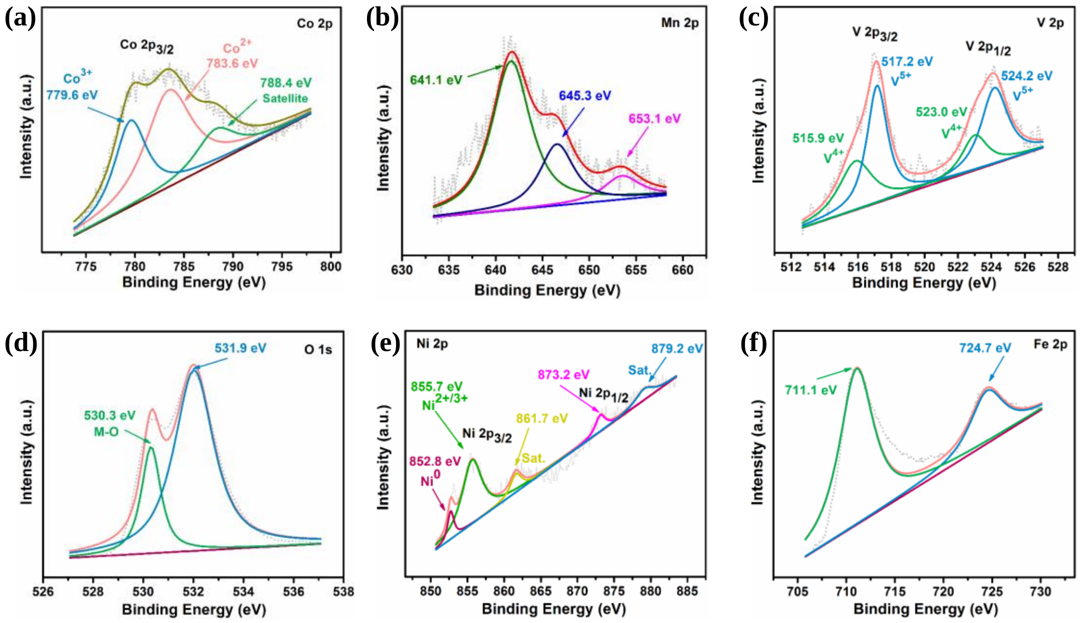

Figure 5.12. Deconvoluted XPS of the tribofilm generated on the wear track in the presence of PO blended with NiO/C-MVO after ASTM D4172 test (a) Co 2p, (b) Mn 2p, (c) V 2p, (d) O 1s (e) Ni 2p and (f) Fe 2p

5.3.5. Tentative lubrication mechanism

The proposed synergistic lubrication mechanism of the NiO/C-MVO nanocomposite as an additive for lubrication can be observed in Figure 5.13. The effectiveness of the additives primarily relies on the composition, longevity, and endurance of the formed tribofilm. The layered structure of C-MVO nanosheets persisted throughout the lubrication process, leading to an increased ease of sliding motion. Cobalt doping in MVO nanosheets has further improved lubrication due to the creation of defects. These defects are recognized for establishing slip systems that influence the electronic structure, ultimately leading to a reduction in shear strength.[6,9,10] Alternatively, the NiO nanospheres amid the layers of C-MVO serve as spacers, effectively averting direct contact between the steel balls and also reducing the agglomeration of C-MVO nanosheets.[6,47] They facilitate the conversion of sliding friction into rolling friction when confronted with the pronounced shear forces produced by the moving balls.[47] This mechanism bears resemblance to micro-bearings and significantly lowers the COF.[47] In summary, the distinctive structure and morphology of the NiO/C-MVO nanocomposite enable it to effectively harness the benefits of both additives when employed as additives in lubricating oil and exhibit remarkable anti-wear and anti-friction properties.

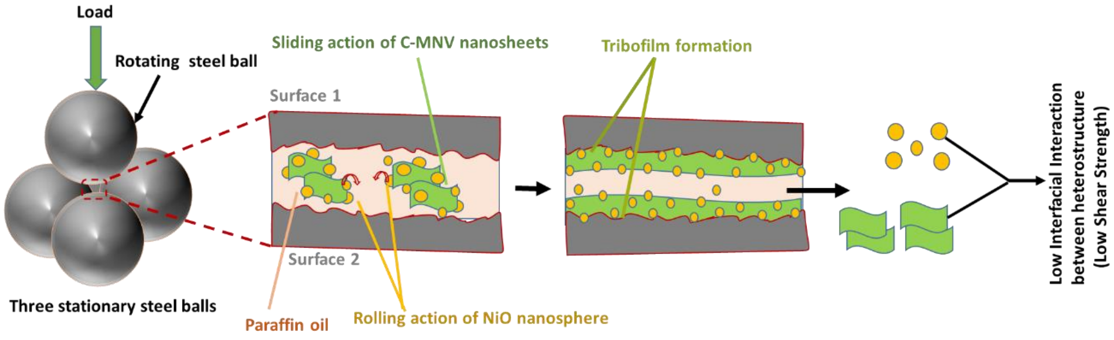

Figure 5.13. The diagrammatic representation of the proposed lubricating mechanism

5.4. CONCLUSIONS

MnV_2O_6 (MVO) and Co-doped MnV_2O_6 (C-MVO) nanosheets were hydrothermally prepared to fabricate exceptionally tribologically efficient materials. The presence of weak van der Waals forces among the nanosheets seems to have a significant impact in the field of tribology. The wilful incorporation of Co as a dopant was aimed at exploiting its potential to augment tribological activity. Undoubtedly, the persistent issues of poor dispersion stability, weak adherence, and agglomerating tendencies of nanosheets exist; the solution to these problems is offered through the non-covalent functionalization of C-MVO nanosheets. MOF-derived NiO nanospheres, prepared through a hydrothermal process followed by calcination, were employed to enhance the tribological performance of C-MVO nanosheets through non-covalent functionalization. The prepared additives were examined using XRD, FT-IR, SEM/HR-SEM, TEM/HR-TEM, and XPS. The HR-SEM and TEM studies of hybrid NiO/C-MVO revealed NiO nanospheres uniformly embedded amidst the layered C-MVO nanosheets. The ASTM D4172 and ASTM D5183 standard tests were used to evaluate the tribological properties of pure PO and its mixtures with additives MVO, NiO, C-MVO, and NiO/C-MVO at the optimum concentration of 0.050% w/v. The tribological data, including the coefficient of friction (COF), mean wear scar diameter (MWD), and seizure load, showed the following order of antiwear and antifriction efficiencies:

MVO < NiO < C-MVO << NiO/C-MVO

Combining the structural benefits of 2D C-MVO lamellae and 0D NiO nanospheres, this nanocomposite achieves a synergistic effect, enhancing tribology performance as a lubricating additive. SEM and AFM investigations of the wear pathway corroborate the above claim. Investigations of the wear track via EDX and XPS studies indicate the generated tribofilm comprised of lubricious metal oxides; Co_2O_3, Co_3O_4, VO_2, V_2O_5, MnO_2, Mn_2O_3, NiO, Ni_2O_3 and metallic alloy Ni-Fe/Cr, which prevents metal-metal contact between sliding surfaces. As a result, the collaborative lubrication provided by C-MVO nanosheets and NiO nanospheres demonstrates outstanding antiwear and antifriction performance.

5.5. REFERENCES

(1) Ye, Q.; Liu, S.; Xu, F.; Zhang, J.; Liu, S.; Liu, W.; Nitrogen-phosphorus co-doped carbon nanospheres as lubricant additives for antiwear and friction reduction. *ACS Appl. Nano Mater.* **2020**, *3*(6), 5362-5371.

(2) Luo, T.; Chen, X.; Wang, L.; Wang, P.; Li, C.; Zeng, H.; Cao, B. Green laser irradiation-stimulated fullerene-like MoS_2 nanospheres for tribological applications. *Tribol.Int.* **2018,** *122*, 119-124.

(3) Song, W.; Yan, J.; Ji, H. Tribological performance of an imidazolium ionic liquid-functionalized SiO_2@ graphene oxide as an additive. *ACS Appl. Mater. Interfaces* **2021,** *13*(42), 50573-50583.

(4) Zhang, X.; Ren, T.; Li, Z. Recent Advances of Two Dimensional Lubricating Materials: from Tunable Tribological Properties to Applications. *J. Mater. Chem. A* **2023**

(5) Zhang, S.; Ma, T.; Erdemir, A.; Li, Q. Tribology of two-dimensional materials: From mechanisms to modulating strategies. *Mater Today*, **2019,** *26*, 67-86.

(6) Shukla, N.; Verma, D.K.; Singh, A.K.; Kumar, B.; Kavita; Rastogi, R.B. Ternary composite of methionine-functionalized graphene oxide, lanthanum-doped yttria nanoparticles, and molybdenum disulfide nanosheets for thin-film lubrication. *ACS Appl. Nano Mater.* **2020**, *3*(8), 8012-8026.

(7) Verma, D.K., Kuntail, J., Kumar, B., Singh, A.K., Shukla, N., Kavita, Sinha, I. and Rastogi, R.B. Amino borate-functionalized reduced graphene oxide further functionalized with copper phthalocyanine nanotubes for reducing friction and

wear. *ACS Appl. Nano Mater.* **2020**, *3*(6), 5530-5541.

(8) Yi, M.; Zhang, C. The synthesis of two-dimensional MoS_2 nanosheets with enhanced tribological properties as oil additives. *RSC adv.* **2018**, *8*(17), 9564-9573.

(9) Shukla, N.; Singh, A.K.; Kavita; Verma, D.K.; Kumar, B.; Maurya, J.L.; Tiwary, D.; Rastogi, R.B. Heterolamellar Bi_2Se_3/Bi_2WO_6 and Bi_2Se_3/N-Doped Bi_2WO_6 Nanosheet Composites as Potential Antifriction and Antiwear Agents. *ACS Appl. Energy Mater.* **2023** *1*(5), 1322-1334.

(10) Singh, A. K.; Shukla, N.; Verma, D. K.; Kavita.; Kumar, B.; Rastogi, R.B. Enhancement of Triboactivity of Nanolamellar Graphitic-C_3N_4 by N-Doped ZnO Nanorods. *Ind. Eng. Chem. Res*. **2021**, *60(2)*, 864-874.

(11) Zhou, C.; Li, Z.; Liu, S.; Zhan, T.; Li, W.; Wang, J. Layered double hydroxides for tribological application: Recent advances and future prospective. *Appl. Clay Sci.* **2022**, *221*, 106466.

(12) Li, Y.F.; Yin, H.; Li, X.L.; Mao, C.C. Friction and Wear Properties of Spark Plasma Sintering NiCr–$SrSO_4$ Composites at Elevated Temperatures in Sliding Against Alumina Ball. *Tribol. Lett.* **2016,** *64*, 1-10.

(13) Zhu, S.; Bi, Q.; Kong, L.; Yang, J.U.; Liu, W. Barium chromate as a solid lubricant for nickel aluminum. *Tribol. Trans.* **2012**, *55*(2), 218-223.

(14) Li, X.B. and Li, Y.F. Tribological Properties of Spark Plasma Sintering TZ_3Y_20A–$SrMoO_4$ Composites at Elevated Temperature. **2017**, *Tribol. Lett. 65*, 1-10.

(15) Liu, E.; Bai, Y.; Gao, Y.; Yi, G.; Jia, J. Tribological properties of NiAl-based

composites containing Ag_3VO_4 nanoparticles at elevated temperatures. *Tribol. Inter.* **2014**, *80*, 25-33.

(16) Chen, Y.S.; Lin, L.Y.; Ma, J.S. Synthesizing molybdenum-doped bismuth vanadate nanoneedle array as photocatalyst for water oxidation using bifunctional molybdenum as dopant and structure directing agent. *Electrochim. Acta* **2020**, *329*, 135171.

(17) Mali, S.S.; Park, G.R.; Kim, H.; Kim, H.H.; Patil, J.V.; Hong, C.K. Synthesis of nanoporous Mo: $BiVO_4$ thin film photoanodes using the ultrasonic spray technique for visible-light water splitting. *Nanoscale Adv.* **2019**. *1*(2), 799-806.

(18) Qi, J.; Kong, D.; Liu, D.; Pan, L.; Chen, Y.; Zhang, X.; Zou, J.J. Bimetallic phosphide decorated Mo–$BiVO_4$ for significantly improved photoelectrochemical activity and stability. *RSC adv.* **2019**, *9*(27), 15629-15634.

(19) Ouyang, J.H.; Li, Y.F.; Zhang, Y.Z.; Wang, Y.M.; Wang, Y.J. High-temperature solid lubricants and self-lubricating composites: A critical review. **2022**, *Lubricants*, *10*(8), 177.

(20) Zhang, W.; Du, L.; Lan, H.; Huang, C.; Zhang, W. Wear behavior of a NiCr/$AgVO_3$ self-lubricating composite. *Acta Metall. Sin.* **2013,** *26*, 435-440.

(21) Liu, E.; Bai, Y.; Gao, Y.; Yi, G.; Jia, J. Tribological properties of NiAl-based composites containing Ag_3VO_4 nanoparticles at elevated temperatures. *Tribol. Inter.* **2014**, *80*, 25-33.

(22) Fengzhen, L.I.U.; Xin, S.H.A.O.; Yibin, Y.I.N.; Limin, Z.H.A.O.; Zhuwei, S.H.A.O.; Xuehua, L.I.U.; Xianhua, M.E.N.G. Shape controlled synthesis and

tribological properties of $CeVO_4$ nanoparticles as lubricating additive. *J. Rare Earths* **2011**, *29*(7), 688-691.

(23) Singh, A.K.; Shukla, N.; Kumar, B.; Verma, D.K.; Maurya, J.L.; Singh, S.; Rastogi, R.B. Improvement of tribo-active behavior of g-C_3N_4 nanosheets using m-$LaVO_4$ nanoparticles. *Colloids Surf. A Physicochem. Eng. Asp.* **2023**, *663*, 131031.

(24) Hua, K.; Li, X.; Fu, Z.; Fang, D.; Bao, R.; Yi, J.; Luo, Z. Cation-exchange synthesis of manganese vanadate nanosheets and its application in lithium-ion battery. *J. Solid State Chem.* **2019**, *273*, 287-294.

(25) Low, W.H.; Lim, S.S.; Siong, C.W.; Chia, C.H.; Khiew, P.S. One dimensional MnV_2O_6 nanobelts on graphene as outstanding electrode material for high energy density symmetric supercapacitor. **2021**, *Ceram. Int. 47*(7), 9560-9568.

(26) Venkatesh, K.; Arumugam, B.; Chen, S.M.; Velmurugan, S.; Subburaj, S.; Hahn, Y.B. Ramaraj, S.K. Synthesis and characterization of manganese vanadate nanopebbles: as energetic electrode material for trichlorophenol detection and supercapacitor applications. *J. Energy Storage*, **2023**, *59*, 106385.

(27) Luo, L. and Maggard, P.A. Effect of ligand coordination on the structures and visible-light photocatalytic activity of manganese vanadate hybrids. *Cryst. Growth Des.* **2013**, *13*(12), 5282-5288.

(28) Pei, L.Z.; Pei, Y.Q.; Xie, Y.K.; Fan, C.G.; Yu, H.Y. Synthesis and characterization of manganese vanadate nanorods as glassy carbon electrode modified materials for the determination of L-cysteine. *CrystEngComm*. **2013**, *15*(9), 1729-1738.

(29) Verma, D. K.; Shukla, N.; Kumar, B.; Singh, A. K.; Shahu, K.; Yadav, M.; Rhee, K. Y.; Rastogi, R. B. Synergistic Tribo-Activity of Nanohybrids of Zirconia/Cerium-Doped Zirconia Nanoparticles with Nano Lamellar Reduced Graphene Oxide and Molybdenum Disulfide. *Nanomaterials* **2020**, *10*, 707-726.

(30) Verma, D. K.; Kumar, B.; Kavita.; Rastogi, R. B. Zinc oxide-and magnesium-doped zinc oxide-decorated nanocomposites of reduced graphene oxide as friction and wear modifiers. *ACS Appl. Mater. Interfaces* **2018**, *11(2)*, 2418-2430.

(31) Singh, A. K.; Shukla, N.; Verma, D. K.; Kumar, B.; Mandal, K. D.; Rastogi, R.B. Reinforcement of nanoporous lanthanum-doped zinc borate by vanadium selenide nanosheets for improved tribological activity. *RSC Adv.* **2022**, *12(29)*, 18685-18696.

(32) Yao, Y.; McDowell, M.T.; Ryu, I.; Wu, H.; Liu, N.; Hu, L.; Nix, W.D.; Cui, Y. Interconnected silicon hollow nanospheres for lithium-ion battery anodes with long cycle life. *Nano letters*, **2011**, *11*(7), 2949-2954.

(33) Cao, C.Y.; Guo, W.; Cui, Z.M.; Song, W.G.; Cai, W. Microwave-assisted gas/liquid interfacial synthesis of flowerlike NiO hollow nanosphere precursors and their application as supercapacitor electrodes. *J. Mater. Chem.* **2011**, *21*(9), 3204-3209.

(34) Lin, G.; Zheng, J.; Xu, R. Template-free synthesis of uniform CdS hollow nanospheres and their photocatalytic activities. *J. Phys. Chem. C* **2008**, *112*(19), 7363-7370.

(35) Li, C.; Liu, Y.; Li, L.; Du, Z.; Xu, S.; Zhang, M.; Yin, X.; Wang, T. A novel amperometric biosensor based on NiO hollow nanospheres for biosensing

glucose. *Talanta* **2008**, *77*(1), 455-459.

(36) Park, J.; Shen, X.; Wang, G. Solvothermal synthesis and gas-sensing performance of Co_3O_4 hollow nanospheres. *Sens. Actuators B: Chem.* **2009**, *136*(2), 494-498.

(37) Kumar, B.; Verma, D.K.; Singh, A.K.; Kavita; Shukla, N.; Rastogi, R.B. Nanohybrid Cu@C: synthesis, characterization and application in enhancement of lubricity. *Compos. Interfaces* **2020**, *27*(8), 777-794.

(38) Xue, M.Q.; Wang, Z.P.; Yuan, F.; Luo, G.S.; Zhang, X.H.; Wei, W.; Tang, H.; Li, C.S. Template-free synthesis of $MoSe_2$ hollow nanospheres with excellent tribological properties. *Chalcogenide Lett*. **2017**, *14*, 37-42.

(39) Ye, Q.; Liu, S.; Zhang, J.; Xu, F.; Zhou, F.; Liu, W. Superior lubricity and antiwear performances enabled by porous carbon nanospheres with different shell microstructures. *ACS Sustain. Chem. Eng.* **2019**, *7*(14), 12527-12535.

(40) Song, H.; Huang, J.; Jia, X.; Sheng, W. Facile synthesis of core–shell Ag@ C nanospheres with improved tribological properties for water-based additives. *New J. Chem.* **2018**, *42*(11), 8773-8782.

(41) Boshui, C.; Kecheng, G.; Jianhua, F.; Jiang, W.; Jiu, W.; Nan, Z. Tribological characteristics of monodispersed cerium borate nanospheres in biodegradable rapeseed oil lubricant. *Appl. Surf. Sci*. **2015**, *353*, 326-332.

(42) Xu, Y., Geng, J., Peng, Y., Liu, Z., Yu, J. and Hu, X., Lubricating mechanism of Fe_3O_4@ MoS_2 core-shell nanocomposites as oil additives for steel/steel contact. *Tribol. Inter*. **2018**, *121*, 241-251.

(43) Çomakli, O.; Yazici, M.; Yetim, T.; Yetim, F.; Celik, A. Tribological and

electrochemical behavior of Ag_2O/ZnO/NiO nanocomposite coating on commercial pure titanium for biomedical applications. *Ind. Lubr. Tribol.* **2019**, *71*(10), 1166-1176.

(44) Rajabi, M.R.; Tahmasebi, K.; Ehteshamzadeh, M.; Soroushian, S. Tribological and magnetic behaviour of Ni-P coating modified with NiO nanoparticles. *Tribol. Mater. Surf. Interfaces* **2021**, *15*(4), 243-251.

(45) Senniangiri, N.; Manikandan, S.; Dhayanithi, G.; Hariharashayee, D.; Chelladurai, C.; Sunil, J. The lubricating properties of Graphene-NiO/Coconut oil hybrid nanofuids. *Mater. Today: Proc.* **2021,** *46*, 3851-3854.

(46) Wang, H.; Yan, L.; Liu, D.; Wang, C.; Zhu, Y.; Zhu, J. Investigation of the tribological properties: Core-shell structured magnetic Ni@NiO nanoparticles reinforced epoxy nanocomposites. *Tribol. Inter.* **2015**, *83*, 139-145.

(47) Li, W.; Luo, T.; Zhu, C.; Zhang, B.; Cao, B. Graphene/h-BN Nanosheet/Nanosphere Composites Constructed by In Situ Laser Irradiation with Synergistically Improved Tribological Performance. *Ind. Eng. Chem. Res.* **2022**, *62*(1), 435-444.

(48) Zhang, X.; Li, X.; Jiang, F.; Du, W.; Hou, C.; Xu, Z.; Zhu, L.; Wang, Z.; Liu, H.; Zhou, W.; Yuan, H. Improved electrochemical performance of 2D accordion-like MnV_2O_6 nanosheets as anode materials for Li-ion batteries. *Dalton Trans.* **2020**, *49*(6), 1794-1802.

(49) Wu, M.K.; Chen, C.; Zhou, J.J.; Yi, F.Y.; Tao, K.; Han, L. MOF–derived hollow double–shelled NiO nanospheres for high–performance supercapacitors. *J. Alloys*

Compd. **2018**, *734*, 1-8.

(50) Chu L.; Li M.; Li X.; Wang Y.; Wan Z., Dou S.; Song D.; Li Y.; Jiang B. High performance NiO microsphere anode assembled from porous nanosheets for lithium-ion batteries. *RSC Adv*. **2015**, *5*(61), 49765-49770.

(51) Kotta, A.; Kim, E. B.; Ameen, S.; Shin, H. S.; Seo, H. K. Communication-Ultra-small NiO nanoparticles grown by low-temperature process for electrochemical application. *J. Electrochem. Soc.* **2020**, *167*(16), 167517.

(52) Nithya, M.; Vidhya, S. A novel g-C_3N_4/MnV_2O_6 heterojunction photocatalyst for the removal of methylene blue and indigo carmine. *Chem. Phys. Lett.* **2019**, *737*, 136832.

(53) Dam, D. T.; Lee, J. M. Polyvinylpyrrolidone-assisted polyol synthesis of NiO nanospheres assembled from mesoporous ultrathin nanosheets. *Electrochim. Acta* **2013**, *108*, 617-623.

(54) Kumar, S.; Das, J. Synthesis, structural and magnetic properties of NiO nanospheres and rGO-NiO nanocomposites and observing magnetocaloric effect in rGO-NiO nanocomposites. *Mater. Sci. Eng. B* **2021**, *265*, 115007.

(55) Ashok, A.; Kumar, A.; Tarlochan, F. Surface alloying in silver-cobalt through a second wave solution combustion synthesis technique. *Nanomater.* **2018**, *8*(8), 604.

(56) Singh, A. K.; Yadav, A.; Indra, A.; Rastogi, R. B. Superior performance of ultrathin metal organic framework nanosheets for antiwear and antifriction testing. *Colloids Surf. A: Physicochem. Eng.* **2021**, *613*, 126100.s

(57) Blanquart, T.; Niinistö, J.; Gavagnin, M.; Longo, V.; Heikkilä, M.; Puukilainen,

E.; Pallem, V. R.; Dussarrat, C.; Ritala, M.; Leskelä, M. Atomic layer deposition and characterization of vanadium oxide thin films. *RSC advances* **2013**, *3*(4), 1179-1185.

(58) Wang, L.; Liu, W.; Wang, X. The preparation and tribological investigation of Ni–P amorphous alloy nanoparticles. *Tribol. Lett.* **2010**, *37*, 381-387.

(59) Li, J.; Xiong, D. Tribological behavior of graphite-containing nickel-based composite as function of temperature, load and counterface. *Wear* **2009**, *266*(1-2), 360-367.

(60) Zheng, X.; Zhang, Y.; Liu, H.; Fu, D.; Chen, J.; Wang, J.; Zhong, C.; Deng, Y.; Han, X.; Hu, W. In situ fabrication of heterostructure on nickel foam with tuned composition for enhancing water-splitting performance. *Small* **2018**, *14*(50), 1803666.

(61) Zhu, Y.; Liu, T.; Li, L.; Song, S.; Ding, R. Nickel-based electrodes as catalysts for hydrogen evolution reaction in alkaline media. *Ionics* **2018**, *24*(4), 1121-1127.